



## Research Article

## Significant “smaller is softer” in amorphous silicon via irradiation-mediated surface modification

Yuecun Wang<sup>a,1</sup>, Lin Tian<sup>b,1</sup>, Meng Li<sup>a,c</sup>, Zhiwei Shan<sup>a,\*</sup><sup>a</sup> Center for Advancing Materials Performance from the Nanoscale (CAMP-Nano) & Hysitron Applied Research Center in China (HARCC), State Key Laboratory for Mechanical Behavior of Materials, Xi'an Jiaotong University, Xi'an 710049, China<sup>b</sup> Institute of Materials Physics, University of Göttingen, Göttingen 37077, Germany<sup>c</sup> Department of Chemical and Petroleum Engineering, University of Pittsburgh, Pittsburgh, PA 15216, United States of America

## ARTICLE INFO

## Article history:

Received 30 January 2023

Revised 11 April 2023

Accepted 28 April 2023

Available online 12 June 2023

## Keywords:

Amorphous silicon

Micropillars

“Smaller is softer”

Ion irradiation

## ABSTRACT

“Smaller is softer” is a reverse size dependence of strength, defying the “smaller is stronger” tenet. It usually results from surface-mediated displacive or diffusive deformation and is mainly found in some ultra-small-scale (below tens of nanometers) metallic materials. Here, making use of the surface modification via ion beam irradiation, we bring the “smaller is softer” into being in a covalently-bonded, hard, and brittle material-amorphous Si (a-Si) at a much larger size regime ( $< \sim 500$  nm). It is manifested as the transition from the quasi-brittle failure to the homogeneous plastic deformation as well as the decreasing yield stress with sample volume reduction at the submicron-scale regime. An analytical model of hard core/superplastic shell has been proposed to explain the artificially-controllable size-dependent softening. This surface engineering pathway via ion irradiation is not only of particular interest to tailor the strength and deformation behaviors in small-sized a-Si or other covalently-bonded amorphous solids but also of practical relevance to the utility of a-Si in microelectronics and microelectromechanical systems.

© 2023 Published by Elsevier Ltd on behalf of The editorial office of Journal of Materials Science &amp; Technology.

## 1. Introduction

There is a general trend of the size-strength relationship in most materials, i.e., “smaller is stronger” [1,2], and the upper bound of the strength increase is the theoretical limit [3]. This is not the whole story in the size regime where physical dimension matters, if we further reduce the material or sample dimension, a size-dependent softening begins to take over at room temperature, manifested as the reduction in the applied stress for initiating plastic deformation with the decreasing size, i.e., “smaller is softer” [4,5]. The “smaller is softer” size effect is of practical interest for some very hard but brittle materials (such as the covalently bonded solids), since the reduction in the stress for initiating plastic deformation with decreasing dimensions makes it feasible to achieve a suitable combination of strength and plasticity [6–8]. Up to now, however, no such a trend has been found in these materials. For metallic materials, of which the size effect in strength and deformability has been fully understood,

the “smaller is softer” arises primarily from the grain boundary or surface-mediated displacive and diffusion processes when the grain size or tested sample dimension decreases down to tens of nanometers [5,9,10]. However, for the inorganic nonmetallic materials with much stronger covalent bonding, the diffusion-dominant or surface-mediated deformation is hardly accessible at ambient temperature even in the very small tested volume below tens of nanometers [11–14]. Here a question naturally arises, how to make size-dependent softening feasible in hard and brittle materials.

For the purpose posted above, we resort to modulating the surface property of small-scale free-standing samples, such that (i) the near-surface regions which are usually perceived as the preferred initiation sites of brittle cracking become “blunt and ductile”; (ii) the surface-mediated deformation can come into play and become increasingly dominant with decreasing dimensions, just as in small enough metallic materials. One feasible way to do this is to irradiate samples using an ion beam, as ion irradiation has been found to be capable of making the creep-like plastic deformation at room temperature possible in some ceramic and semiconductor materials [15–19]. Via imposing nanoscale ion-matter interaction on material surfaces, microstructures and interatomic bonds can be manipulated [15,20], and with the sample size reduction, the contribution of the surface to the overall mechanical behavior becomes

<sup>\*</sup> Corresponding author.E-mail address: [zwshan@xjtu.edu.cn](mailto:zwshan@xjtu.edu.cn) (Z. Shan).<sup>1</sup> These authors contributed equally to this work.

more and more significant. We, therefore, carried out quantitative uniaxial compression testing of the focused-ion-beam-irradiated amorphous Si (a-Si) pillars with varied sizes at micro- and nano-scales, feasible using a quantitative nanomechanical testing system inside electron microscopes. Here the choice of a-Si is made, in lieu of crystals or compounds, mainly due to the following reasons: (i) to avoid complications owing to the crystal anisotropy, variable slip systems, chemical composition, etc.; (ii) besides being the classic covalent bonded amorphous material [21–23], a-Si is also one of the most important semiconductors and has been used as the structural material of Micro/Nano-electromechanical Systems (MEMS/NEMS) devices [24–30]; (iii) a-Si is an intrinsic brittle material even at the nanoscale [31]; (iv) ion beam irradiation itself, which has been routinely used in microelectronics and semiconductor industry as a powerful tool for doping [32–34], surface smoothing, and cleaning [35], is of practical interest for a-Si. In the following, we will demonstrate that the surface-modified a-Si exhibits an apparent “smaller is softer” size effect extending into submicrometre at ambient temperature.

## 2. Experimental

### 2.1. Deposition of a-Si film

The a-Si films were deposited to a wedge-shaped Si substrate (110  $\mu\text{m}$  height, 8  $\mu\text{m}$  top width) via the Plasma Enhanced Chemical Vapor Deposition (PECVD). The wedge-shaped substrate was selected to avoid the electron beam being blocked during the compression of pillars inside the scanning electron microscope (SEM) and transmission electron microscope (TEM). The deposition parameters are as follows: radio frequency (RF) power = 20 W, substrate temperature = 250  $^{\circ}\text{C}$ , process pressure = 800 mTorr,  $\text{SiH}_4$  flow rate = 30 sccm, Ar flow rate = 475 sccm. The deposited a-Si film with a thickness of about 11  $\mu\text{m}$  adheres firmly to the substrate surface, and no hillocks or big voids have been found in the a-Si film during the layer-by-layer focused ion beam (FIB) milling process.

### 2.2. Nanoindentation tests on a-Si film

Nanoindentation tests were carried out by the Bruker–Hysitron TriboIndenter 950 with a diamond Berkovich nano-indenter. A-Si films ( $\sim 11 \mu\text{m}$  thick) deposited on the wedge-shaped single-crystalline silicon substrate were compressed under the load-control mode with the constant loading/unloading rate of 20  $\mu\text{N/s}$  (quasi-static loading) to the peak loads of 600  $\mu\text{N}$  for the 2 s holding time. The nanoindentation depth (tens of nanometers) is much smaller compared with the thickness of a-Si film ( $\sim 11 \mu\text{m}$ ), and hence the influence from the crystalline Si substrate can be ignored.

### 2.3. Microfabrication of a-Si pillars for the uniaxial compression tests

The a-Si pillars with the nominal diameter  $d$  (at half height) ranging from  $\sim 80 \text{ nm}$  to  $\sim 2 \mu\text{m}$  and aspect ratio (defined as the height to diameter) 2–3 were micromachined by the 30 keV focused  $\text{Ga}^+$  ions beam (Field Electron and Ion Company (FEI) Helios NanoLab 600 dual-beam FIB system) directly from the deposited a-Si film. In the microfabrication process of pillars, the used ion beam current for coarse cutting was in the range of 9.3–2.8 nA, and the beam current for the final fine polishing was sequentially decreasing from 280 pA to 1.5 pA. To avoid the pillars' top-rounding induced untimely yielding at a low stress, we rotated the sample by  $180^{\circ}$  after a pillar was milled to the target diameter, tilted into the pillar  $1^{\circ}$ – $2^{\circ}$ , and cut its round top. The a-Si pillars for control experiments were further sequentially milled by the

5 keV focused gallium ion beam as well as the low-energy argon ion beam (2 keV, 1 keV, and 0.2 keV, in the Fischione Model 1040 NanoMill system) after the 30 keV high-energy focused gallium ion beam milling.

### 2.4. Uniaxial compression tests inside SEM and TEM

Given the large studied size range, the uniaxial compression tests were conducted with the Bruker–Hysitron TEM PicoIndenter PI95 (for small size pillars 80–400 nm) and Bruker–Hysitron SEM PicoIndenter PI87 (for the bigger size pillars 200–2000 nm) inside TEM as well as SEM. For the big a-Si pillars, the forces they required for yielding are large and out of the 1.5 mN limit of Bruker–Hysitron PI95 TEM PicoIndenter. Therefore, they were tested inside the FIB chamber by PI87 SEM PicoIndenter, of which the maximum load is 15 mN. When the samples are small enough (e.g.,  $< 350 \text{ nm}$ ), they can be tested inside TEM, as the forces required are now within the limit of PI95. For all a-Si pillars, their engineering stresses were calculated by dividing the load by cross-section area, which is calculated as  $\pi d^2/4$ . The engineering strain was defined as the ratio of the deformation displacement of the pillar (i.e. the displacement reading minus the contribution from the substrate) to its initial height (the distance from the top to the substrate).

### 2.5. Raman characterizations of a-Si before and after $\text{Ga}^+$ ions irradiation

Raman microspectroscopy characterizations were conducted to study the structural change in the  $\text{Ga}^+$ -ion beam fabricated a-Si lamellas using a HeNe laser with an incident wavelength of 633 nm, using a LabRAM HR Evolution (HORIBA Jobin Yvon) spectrometer with the  $\sim 1 \mu\text{m}$  spatial resolution. The output laser power is controlled below 0.5 mW to avoid heating-induced crystallization in a-Si.

## 3. Results and discussion

### 3.1. Nanoindentation test on a-Si samples with FIB irradiation or not

The focused ion beam (FIB) was chosen because of its powerful ability in the site-specific bombardment and milling, to accomplish the ion irradiation onto the surface and preparation of tested samples in the meantime. We firstly irradiated a-Si film (11  $\mu\text{m}$  thick) using the focused  $\text{Ga}^+$  ions beam (30 keV) to study the mechanical property change upon irradiation. The trajectories of 30 keV  $\text{Ga}^+$  ions into Si were simulated by the stopping and range of ions in matter (SRIM) software [36]:  $\text{Ga}^+$  ions can reach up to  $\sim 40 \text{ nm}$  in the depth direction (as shown in Fig. 1, the upper left inset). To demonstrate the irradiation effect on the mechanical response of a-Si and meanwhile decrease the influence from the un-irradiated substrate as much as possible, the peak loading of 600  $\mu\text{N}$  was selected. The load-displacement curves shown in Fig. 1 compare the a-Si samples with (red) and without (black) FIB irradiation (the dosage of  $\text{Ga}^+$  ions is  $2 \times 10^{16} \text{ ions/cm}^2$ ): under the same nanoindentation loading and unloading, the  $\text{Ga}^+$ -irradiated a-Si has a  $\sim 16 \text{ nm}$  indentation depth with the hardness of  $\sim 12 \text{ GPa}$ , while the FIB-free a-Si only has an indentation depth of  $\sim 6 \text{ nm}$  and the  $\sim 7 \text{ GPa}$  hardness; during the 2 s holding process (at 600  $\mu\text{N}$ ), the former has a 1.5 nm plastic displacement, almost two times larger than that of the latter. The nanoindentation tests unambiguously show the  $\text{Ga}^+$ -irradiated a-Si samples become significantly softened and demonstrate much better plastic deformability compared with the FIB-free ones.

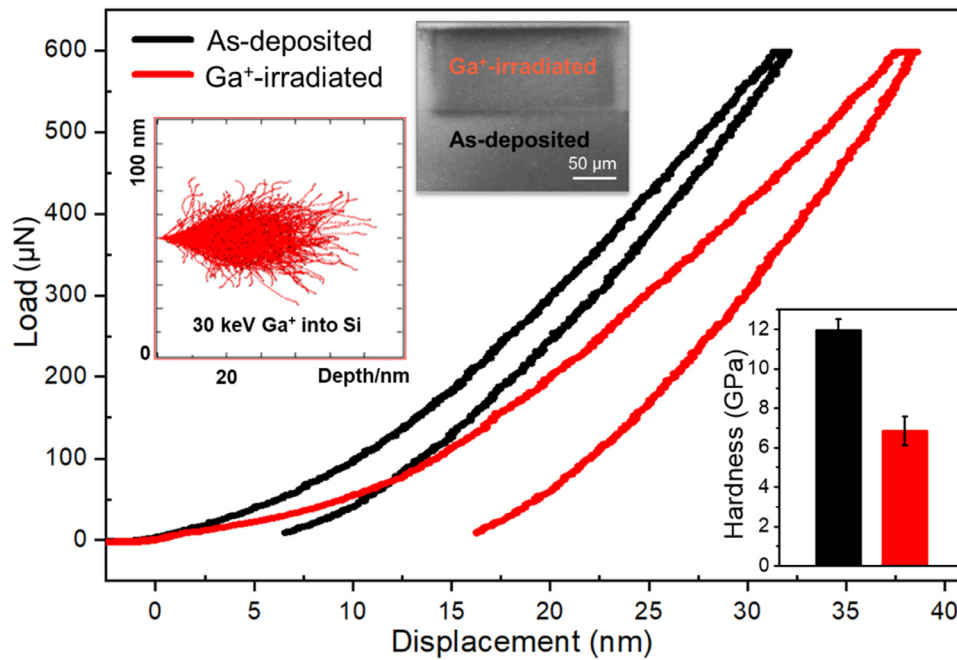


**Fig. 1.** Ga ions irradiation induced softening of a-Si. Load-displacement curves of the  $\text{Ga}^+$ -irradiated (red curve) and FIB-free (as-deposited, black curve) a-Si from the nanoindentation tests. The top left inset shows the simulated trajectories of the 30 keV  $\text{Ga}^+$  ions irradiation into Si using the stopping and range of ions in matter (SRIM) software. The inset SEM image demonstrates the  $\text{Ga}^+$ -irradiated zone and the as-deposited zone on a-Si film. The lower right inset compares the nanoindentation hardness of a-Si with (red) and without (black) FIB irradiation.

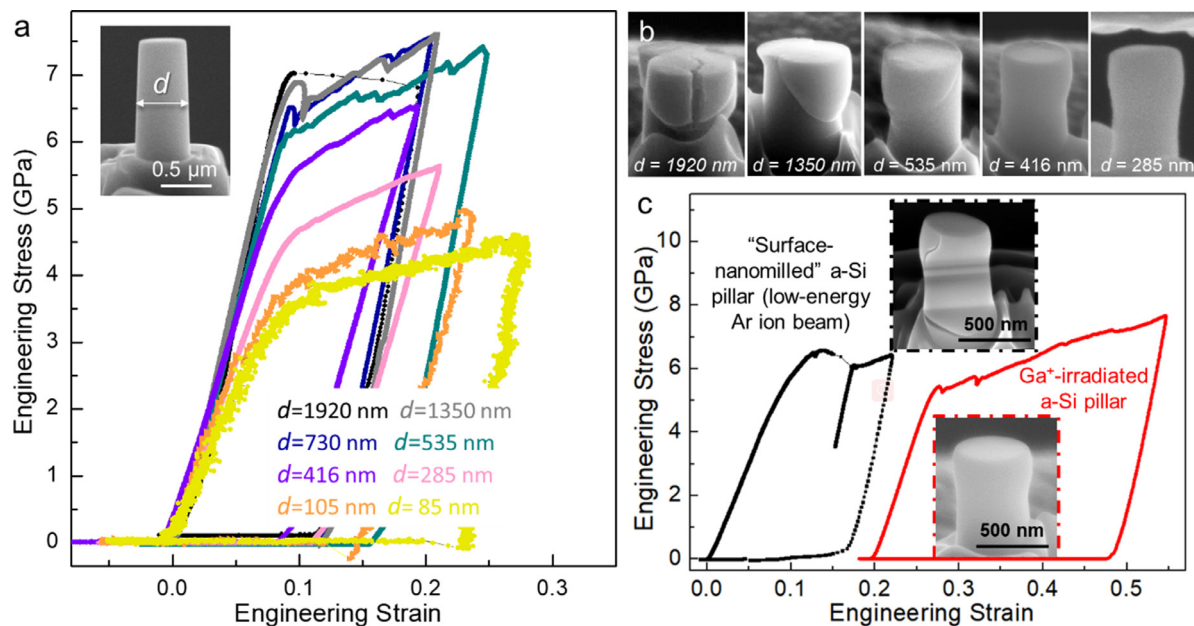


**Fig. 2.** Strength reduction and brittle-to-ductile transition in ion-beam-irradiated a-Si pillars with decreased size. (a) Representative engineering stress–strain curves of the ion-beam-irradiated a-Si pillars with varied diameters. The inset shows the SEM image of an a-Si pillar with the nominal diameter  $d$  (at half height). (b) Morphologies of compressed a-Si pillars with decreasing diameters from left to right, showing the intermittent-to-homogeneous transition in deformation mode. (c) Comparisons of the engineering stress–strain curves and compressed morphologies of the as- $\text{Ga}^+$ -irradiated a-Si pillar ( $d = 486$  nm) and the surface-nanomilled a-Si pillar ( $d = 405$  nm).

### 3.2. Uniaxial compression on the $\text{Ga}^+$ -irradiated a-Si pillars

a-Si pillars with a nominal diameter  $d$  ranging from 80 nm to  $\sim 2$   $\mu\text{m}$  and aspect ratios of 2–3 were micromachined by FIB directly from the deposited a-Si film. This size range was selected because most of the small-volume solids in this regime demonstrate a “smaller is stronger” trend according to our conventional wisdom. The inset in Fig. 2(a) shows the scanning electron microscope (SEM) image of a typical a-Si pillar. By controlling the cur-

rent density of the ion beam and the milling time of the final-step fine polishing [18], the dosages of  $\text{Ga}^+$  ions into all a-Si pillars keep in the same order of  $\sim 10^{16}$  ions/ $\text{cm}^2$ . These a-Si pillars were compressed using a quantitative nanomechanical testing system, and the loading was performed under the displacement-control mode with the constant strain rate in the range of  $10^{-3}/\text{s}$  to  $10^{-2}/\text{s}$ , i.e., quasi-static loading. Fig. 2(a) demonstrates the representative engineering stress–strain curves of a-Si pillars with varied diameters. For pillars with  $d > \sim 1$   $\mu\text{m}$ , “strain bursts”, defined

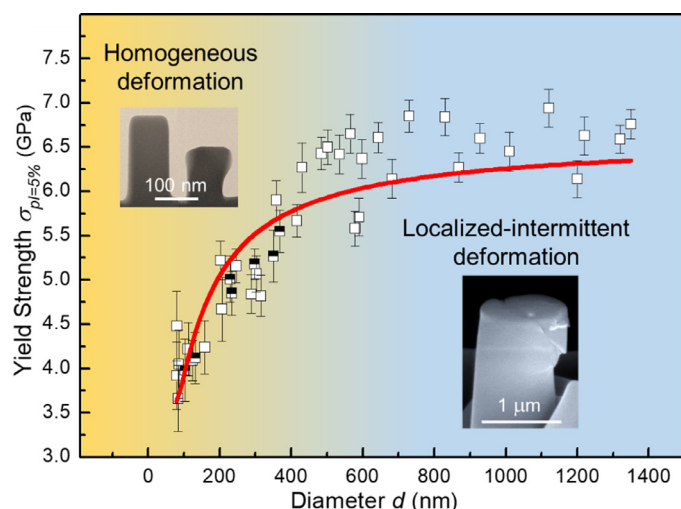


**Fig. 3.** “Smaller is softer” in the Ga-ion-beam-irradiated a-Si pillars. The yield strengths (at 5% plastic strain) as a function of the pillar diameters. Most of the pillars were compressed with an electron beam blocked (the corresponding data is represented by open squares, and the half-up solid squares represent the pillars tested inside TEM with an e-beam on). The red curve is the fitted curve of all data points according to Eq. (4): the strength is an increasing function of decreasing sample size. The top left inset shows the TEM images of a  $d = 85$  nm a-Si pillar before and after compression, showing the homogeneous plastic deformation. The lower right is the SEM image of a compressed pillar ( $d = 1280$  nm) demonstrating an obvious shear-off step (the localized and intermittent deformation).

as the distinguishable separation between the elastic and plastic part at the stress of  $\sim 7$  GPa, can be clearly seen on the engineering stress-strain curves, showing a quasi-brittle failure characteristic (also see their compressed morphologies shown in Fig. 2(b)). With further reduction of  $d$ , the strain jumps are absent and the continuous plastic flow begins to take over. In this case, the flow commences via shear-banding, as again visible in the pillars' morphology after compression, but continues further in a smooth fashion. When  $d$  decreases below  $\sim 500$  nm, a-Si pillars deform homogeneously, showing significantly improved plastic deformability. In the studied size range here from 80 nm–2  $\mu$ m, the transition from elastic to plastic flow (i.e., yielding) sets in at a lower and lower stress with smaller  $d$ , and the flow stress decreases accordingly. It is evident that the smaller samples tend to demonstrate the apparent soft and smooth flow response. To validate that the transition from quasi-brittle failure to plastic flow is mainly attributed to the  $\text{Ga}^+$  irradiation-induced surface softening instead of the sample size reduction, we fabricated some a-Si pillars with a diameter of  $\sim 400$  nm (below the above-mentioned transition size of  $\sim 500$  nm), and then further polished their surface using the low-energy Ar ion beam to minimize the irradiation effect (see Experimental Section 2.4 for more details about the surface nanomilling). It has been reported that the  $\text{Ga}^+$  irradiation-induced damage layer on the Si surface can be reduced to less than 1 nm after the Ar ion beam nanomilling with the energy as low as 0.2 keV [37], which could be neglected for a pillar with a diameter of  $\sim 400$  nm. From the engineering stress-strain curves and compressed morphologies of the surface-nanomilled a-Si pillar and the as- $\text{Ga}^+$ -irradiated a-Si pillar (the diameter of the latter is larger, Fig. 2(c)), we can see that once the  $\text{Ga}^+$ -irradiated surface layer is diminished to an ignorable thickness, the a-Si pillar becomes “brittle” again, i.e., the decreasing diameter of a-Si pillars doesn't mainly account for the enhanced plasticity.

To demonstrate the size-affected strength of  $\text{Ga}^+$ -irradiated a-Si pillars more clearly, Fig. 3 summarizes their yield strength at 5% plastic strain (denoted as  $\sigma_{\text{pl}=5\%}$ ) as a function of  $d$ . The measured yield strength decreases with size reduction, and this change

is more dramatic for smaller pillars ( $d < \sim 500$  nm). Note that the quantitative compression tests were carried out under electron beam (e-beam) imaging. To avoid the possible heating and radiolysis effects from the e-beam, especially for the smaller-sized samples compressed inside TEM (200 keV), the e-beam was blocked after positioning the punch near the sample. Most of the a-Si pillars were tested with e-beam off (represented by the open squares in Fig. 3), and some pillars (the half-up solid squares) were tested under the e-beam illumination inside TEM (e-beam intensity  $\leq 2 \times 10^{-2}$  A/cm<sup>2</sup>). The discrepancy of measured yield strengths under e-beam on and off conditions is within the margin of error, suggesting that the e-beam effect can be negligible here. Together with the “smaller is softer” trend in strength, the apparent intermittent-to-homogeneous or “brittle-to-plastic” transition occurs: the pillars ( $d > \sim 500$  nm) with obvious shear steps formed during “strain jumps”, which correspond to the intermittent kinetics of shearing-banding, show a shear-band-dominated localized plastic deformation; whilst the deformation appears predominantly homogeneous when  $d$  decreases below  $\sim 500$  nm, featuring the mushroom-like shape (Fig. 2(b)) and consistent with their continuous stress-strain curves (Fig. 2(a)).

### 3.3. Characterizations of the $\text{Ga}^+$ -irradiated a-Si

To understand the ion beam irradiation-mediated softening of a-Si pillars, we first characterized the  $\text{Ga}^+$ -affected surface. The high-resolution TEM (HRTEM) image of an a-Si pillar ( $d = 150$  nm, Fig. 4(a)) clearly shows the amorphous nature of the whole pillar without obvious crystallization, a rather smooth surface, as well as the absence of a visible boundary between the irradiated surface and the unaffected inner zone. No obvious differences can be seen from the HRTEM images, which show the typical maze-like contrast of amorphous solids, as well as the corresponding Fast Fourier Transforms (FFTs) of the a-Si thin film before and after  $\text{Ga}^+$  irradiation (Fig. 4(b, c)). Considering that both the  $\text{Ga}^+$ -irradiated a-Si and its irradiation-free counterpart are amorphous, high-resolution TEM characterizations may not demonstrate the structural change. Therefore, Raman spectroscopy, the spectrum of which is sensitive to the structural defects and bonding variations in a-Si [38], was used. The inset in Fig. 4(d) shows the schematic of three a-Si cuboid samples (4  $\mu$ m wide and 4  $\mu$ m high) finely milled by FIB to the thicknesses of 2000 nm, 1000 nm, and 200 nm, respectively. The thinning process was equivalent to that for the fabrication of a-Si pillars. The incident laser (wavelength of 633 nm) with a probe size of 2  $\mu$ m for Raman spectroscopic characterization is perpendicular to the through-thickness direction of samples. To avoid possible crystallization of a-Si caused by the laser heating, the laser power was controlled as low as possible ( $< 0.5$  mW). The penetration depth of the 633 nm laser into Si is about 3  $\mu$ m [39,40], larger than the thickness of all tested samples. Raman spectrums of the  $\text{Ga}^+$ -irradiated and reference FIB-free a-Si samples are shown in Fig. 4(d). The transverse optical (TO) peak with the wavenumbers of  $\sim 470$  cm<sup>-1</sup> is concerned specifically. Compared with the FIB-free one, three  $\text{Ga}^+$ -irradiated samples demonstrate a TO peak position shift towards lower wavenumbers (negative Raman shift). The 200 nm thick a-Si specimen has the highest Raman shift value of 8.2 cm<sup>-1</sup> (the red curve). The increasing negative Raman shift value with the thickness reduction of a-Si samples agrees well with the trend of volume fraction of the  $\text{Ga}^+$ -irradiated layers (Fig. 4(e)) in each sample. Here the average thickness of the FIB-affected layer is regarded to be 40 nm from the SRIM simulation result of the 30 keV  $\text{Ga}^+$  ions into Si (inset in Fig. 1) as well as the fitted value of 39.8 nm according to a core-shell analytical model and our experimental data (see Section 3.4 below).



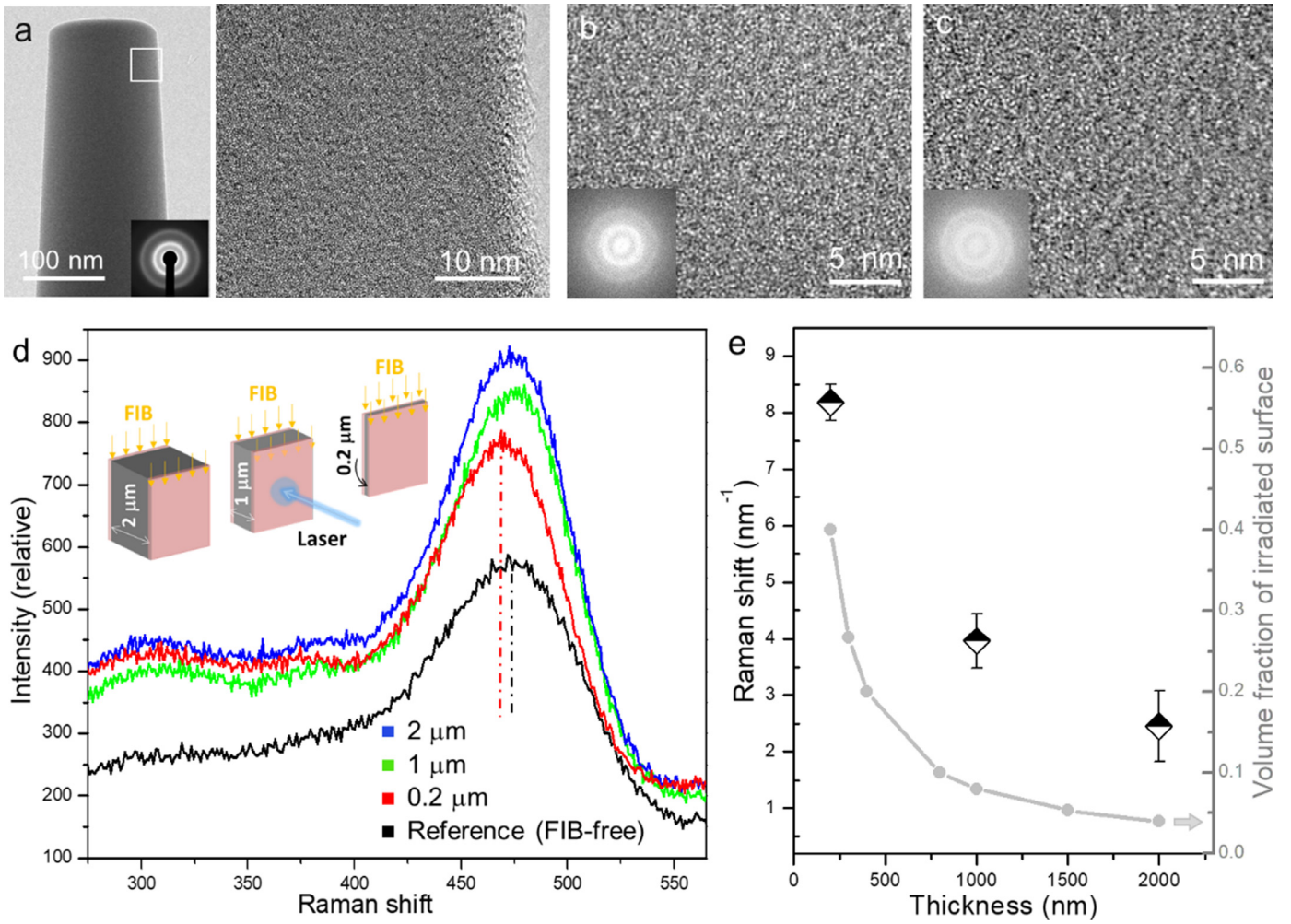


**Fig. 4.** Characterizations of the  $\text{Ga}^+$ -irradiated a-Si. (a) Bright-field TEM image of a typical a-Si pillar fabricated & irradiated by a focused gallium ion beam, as well as the HRTEM image of the white-framed zone of the pillar. HRTEM images of the a-Si thin film ( $\sim 50$  nm in thickness) before (b) and after (c)  $\text{Ga}^+$  irradiation. (d) Raman spectra of the  $\text{Ga}^+$ -irradiated a-Si samples with different thicknesses as well as the FIB-free sample (the black curve). The upper left inset shows the schematic of the experimental setup: the surface layer in red represents the FIB-affected layer, and the as-grown part is in gray. (e) Raman shift (left, black) and volume fraction of the irradiated surface layer (right, gray) as a function of sample thickness, respectively.

### 3.4. An analytical model of “hard core-soft shell structure”

Based on the above experimental results, the ion-irradiated near-surface region (shell) in the a-Si pillar could be treated as a separate but homogeneous continuum layer with different structures and mechanical behaviors from the unaffected inner part. The most straightforward way of managing this surface effect is depicted in Fig. 5 (the lower left inset), where an analytical core-shell model is considered. According to the rule of mixtures, the yield strength  $\sigma$  of a-Si pillars can be expressed as

$$\sigma = \sigma_{\text{shell}} f_{\text{shell}} + \sigma_{\text{core}} (1 - f_{\text{shell}}) \quad (1)$$

where  $\sigma_{\text{shell}}$  and  $\sigma_{\text{core}}$  are, respectively, the yield strength of ion-irradiated a-Si shell and unaffected a-Si core;  $f_{\text{shell}}$  is the volume fraction of shell in the whole pillar, and according to the core-shell model it approximates

$$f_{\text{shell}} = 1 - \left(1 - \frac{2t}{d}\right)^2 \quad (2)$$

Owing to the shell thickness  $t$  is a constant regardless of pillar diameter  $d$ ,  $\sigma_{\text{shell}}$  is supposed to be a size-independent constant, while the core size,  $d - 2t$ , is tied up with  $d$ . For a-Si, its plastic strain and failure are mediated by the formation of nanoscopic

planar defects, called shear bands (SBs) [41]. Studies on amorphous metals at the micro- and nano-scale tell us that the strength is controlled by the nucleation of the shear band, starting from its embryonic stage: the smaller the sample size, the more difficult this nucleation becomes, following a typical “smaller is stronger” trend [42]. This size dependence can be explained from an energy balance perspective with a resulting power law, according to which we arrived at [42]

$$\sigma_{\text{core}}^2 - \sigma_0^2 = \frac{\psi}{d - 2t} \quad (3)$$

where  $\sigma_{\text{core}}$  is the stress needed to initiate a single shear band, and a main shear band may be the cause for the onset of plastic deformation in a-Si pillars;  $\psi$  is a constant associated with Young’s modulus, a-Si pillar aspect ratio (here assumed a constant of  $\sim 2$ ), and energy per unit area of the shear band. After shear band initiation, the required stress for maintaining the propagation/sliding of the shear band becomes  $\sigma_0$ . It is the resistance against localized severe shearing associated with the shear band itself, and hence it can be deemed independent of sample size [43]. The stress needed for shear band nucleation,  $\sigma_{\text{core}}$ , is sensitive to flaws and hence strongly dependent on sample size. Plugging Eqs. (2) and (3) into

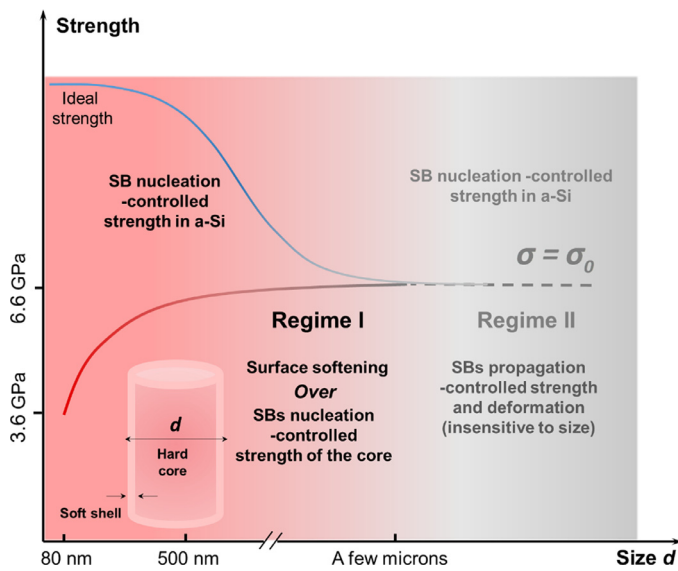


**Fig. 5.** Schematic showing the size-dependent strength trend of a-Si pillars with ion irradiation. Two regimes correspond to different strength-controlling mechanisms. The inset schematically shows the core-shell structure of the ion-irradiated a-Si pillar. With the ion-irradiation-mediated surface modification, the strength of a-Si is no longer an increasing function of decreasing sample size (blue curve) but switches to “smaller is softer” (red curve, Regime I). For large pillars (submicron to a few microns), the surface softening plays an ignorable effect on the mechanical strength, and one arrives at the Regime II, a size-independent plateau (the dashed line).

Eq. (1), the resulting size effect of strength in a-Si is then

$$\sigma = \left(1 - \frac{2t}{d}\right)^2 \cdot \sqrt{\frac{\psi}{d - 2t}} + \sigma_0^2 + \left[1 - \left(1 - \frac{2t}{d}\right)^2\right] \cdot \sigma_{\text{shell}} \quad (4)$$

where  $d$  and  $\sigma$  are the parameters measured experimentally,  $\sigma_0$  is the required stress for maintaining shear band propagation, and assumed to be the average yield strength of micron-sized a-Si pillars (6.6 GPa),  $\psi$  is a constant,  $\sigma_{\text{shell}}$  (the yield strength of ion-irradiated a-Si shell) can be derived by fitting the curve predicated by Eq. (4) to the experimental data in Fig. 3. The fitting curve in red plotted in Fig. 3 agrees well with the measured strength variation, yielding  $\sigma_{\text{shell}} = 3.6$  GPa,  $t = 39.8$  nm. Noted that the measured average yield strength of  $d = \sim 80$  nm a-Si pillars (ion-irradiated near-surface region spans the whole pillar) is about 3.8 GPa, approximating the analytical solution of  $\sigma_{\text{shell}}$ . This consistency validates the core-shell structure model.

### 3.5. Explanation for the significant “smaller is softer”

The analytical results suggest that a-Si pillars are significantly surface-softened by ion irradiation and they can be regarded as the composite material with Ga<sup>+</sup>-irradiated “soft” shell and unaffected “hard” core. Softening and superplasticity of the near-surface regions in a-Si result from the ion-irradiation-induced structural disorders, which serve as fertile sites for plastic flow. Raman TO peak originates from the tetrahedrally-bonded short-range order in the ideal continuous random network structure of a-Si [44], and the measured negative Raman shift from Ga<sup>+</sup>-irradiated a-Si pillars (Fig. 4(d)) indicates the decreased mass density or more structural defects in a-Si [38,45,46]. Structural defects, such as the broken bonds with threefold coordination [47], “point defects”-like dangling bonds and floating bonds, are introduced into the near-surface regions of a-Si pillars during irradiation. The continuous chain reaction of broken bond rearrangements as well as the co-operation effect of these structural defects can facilitate the plastic

events in irradiated a-Si [47,48]. Given the complexity and challenges in characterizing the ion-beam-irradiation-induced structural defects in amorphous materials, more details about these defects (including their atomic-scale structure and formation mechanism) as well as how they act as plasticity carriers in a-Si will be further discussed in a separate paper.

To recapitulate, it has been known that a-Si is an intrinsic brittle material even at the nanoscale [31], and its strength should follow the well-established tenet of “smaller is stronger” till the ideal strength limit (as schematically shown by the blue curve in Fig. 5). Via the ion-irradiation-mediated surface modification, a-Si pillars with the diameter from tens of nanometers to hundreds of nanometers (denoted as Regime I in Fig. 5) demonstrate increasingly enhanced plasticity as the size decreases and the significant “smaller is softer” effect. This can be rationalized as below: the confinement from the thick enough surface-plasticized shell can effectively suppress the nucleation of cracks on near-surface regions as well as their quick propagation across the pillar, and thus the confined core gets the chance to deform plastically via the activation and propagation of SBs; at Regime I (from submicron to nanoscale), with scale down, the stress reduction caused by the quickly increasing volume fraction of the soft shell prevails over the SBs nucleation-controlled strength increase. Therefore, the observed “smaller is softer” and the “brittle-to-ductile” is a “size effect” mainly due to the increasingly large surface-to-volume ratio and surface-assisted homogeneous plastic flow. When one arrives at Regime II (from submicron to a few microns or larger, where the effect from the surface-plasticized can be ignorable), the strength of the a-Si core is SBs propagation dominant and becomes insensitive to sample size, approaching a constant value of  $\sigma_0 = 6.6$  GPa, shown as the plateau in Fig. 5 (the dashed line).

## 4. Conclusion

In summary, making use of the ion-irradiation-mediated surface modification, we switch the conventional “smaller is stronger” size dependence of strength to “smaller is softer” in submicron-sized a-Si, manifested as the deformation mode transition from the quasi-brittle failure to the homogeneous plastic flow as well as the decreasing yield strength along with sample size reduction. Raman spectroscopic characterizations and an analytical core-shell model reveal the underlying mechanism. Ion-irradiation-induced structural defects facilitate the superplastic flow in the affected near-surface region. With size reduction, the softening and confinement effects from the plasticized surface prevail over the SBs nucleation-controlled strength increase and SBs propagation-mediated quasi-brittle failure, showing lower and lower stress for initiating the plastic deformation of a-Si and thus the overall plastic flow of the whole sample. This work may not only shed new light on our understanding of the surface-dominant strength and deformation behaviors in small-volume materials but also inspire a feasible way to tailor their mechanical properties for more reliable and stable micro/nano-structured devices.

## Declaration of Competing Interest

The authors declare that they have no known competing financial interests or personal relationships that could have appeared to influence the work reported in this paper.

## Acknowledgements

The authors acknowledge the support from the National Key R&D Program of China (no. 2022YFB3203600), the National Natural Science Foundation of China (no. 52272162), the China Postdoctoral Science Foundation (Nos. 2021T140535 and 2019M663696), and

the Alexander von Humboldt Foundation. L.T. thanks Dr. Christoph Meyer and Prof. Vasiliy Moshnyaga for their help in Raman spectroscopy measurement. M.L. acknowledges the support from Prof. Xixiang Zhang and the nanofabrication core lab at King Abdullah University of Science and Technology for the nanofabrication facilities.

## References

- [1] M.D. Uchic, D.M. Dimiduk, J.N. Florando, W.D. Nix, *Science* 305 (2004) 986–989.
- [2] Q. Yu, Z.W. Shan, J. Li, X. Huang, L. Xiao, J. Sun, E. Ma, *Nature* 463 (2010) 335–338.
- [3] W.Z. Han, L. Huang, S. Ogata, H. Kimizuka, Z.C. Yang, C. Weinberger, Q.J. Li, B.Y. Liu, X.X. Zhang, J. Li, E. Ma, Z.W. Shan, *Adv. Mater.* 27 (2015) 3385–3390.
- [4] Q.J. Li, E. Ma, *Mater. Res. Lett.* 6 (2018) 283–292.
- [5] S. Yip, *Nature* 391 (1998) 532–533.
- [6] S.W.L. Lucas, A. Berla, I. Ryu, Y. Cui, William D. Nix, *J. Power Sources* 258 (2014) 253–259.
- [7] K. Zheng, C. Wang, Y.Q. Cheng, Y. Yue, X. Han, Z. Zhang, Z. Shan, S.X. Mao, M. Ye, Y. Yin, *Nat. Commun.* 1 (2010) 24.
- [8] M.J. Madou, *Fundamentals of Microfabrication: the Science of Miniaturization*, CRC Press, Boca Raton, 2002.
- [9] L. Tian, J. Li, J. Sun, E. Ma, Z.W. Shan, *Sci. Rep.* 3 (2013) 2113.
- [10] L.H. Jun Sun, Y.C. Lo, T. Xu, H.C. Bi, L.T. Sun, Z. Zhang, S.X. Mao, J. Li, *Nat. Mater.* 13 (2014) 1007–1012.
- [11] Y. Zhu, F. Xu, Q. Qjin, W.Y. Fung, W. Lu, *Nano Lett.* 9 (2009) 3934–3939.
- [12] H. Zhang, J. Tersoff, S. Xu, H. Chen, Q. Zhang, K. Zhang, Y. Yang, C.S. Lee, K.N. Tu, J. Li, *Sci. Adv.* 2 (2016) e1501382.
- [13] Z. Zhang, J. Cui, K. Chang, D. Liu, G. Chen, N. Jiang, D. Guo, *Nanoscale* 11 (2019) 9862–9868.
- [14] Y. He, L. Zhong, F. Fan, C. Wang, T. Zhu, S.X. Mao, *Nat. Nanotechnol.* 11 (2016) 866–871.
- [15] M. Aramesh, Y. Mayamei, A. Wolff, K.K. Ostrikov, *Nat. Commun.* 9 (2018) 835.
- [16] A. Hedler, S.L. Klaumünzer, W. Werner, *Nat. Mater.* 3 (2004) 804.
- [17] Y.C. Wang, D.G. Xie, X.H. Ning, Z.W. Shan, *App. Phys. Lett.* 106 (2015) 081905.
- [18] Y.C. Wang, L. Tian, F. Liu, Y.B. Qin, G. Zheng, J.T. Wang, E. Ma, Z.W. Shan, *Small* 13 (2016) 1601753.
- [19] Y.C. Wang, W. Zhang, L.Y. Wang, Z. Zhuang, E. Ma, J. Li, Z.W. Shan, *NPG Asia Mater.* 8 (2016) e291.
- [20] S. Nakano, S. Muto, T. Tanabe, *Mater. Trans.* 47 (2006) 112–121.
- [21] Y. Wang, J. Ding, Z. Fan, L. Tian, M. Li, H. Lu, Y. Zhang, E. Ma, J. Li, Z. Shan, *Nat. Mater.* 20 (2021) 1371–1377.
- [22] M.M.J. Treacy, K.B. Borisenko, *Science* 335 (2012) 950–953.
- [23] Y. Wang, B. Liang, S. Xu, L. Tian, A.M. Minor, Z. Shan, *Nano Lett.* 20 (2020) 449–455.
- [24] T.M. Howe, R.S. Muller, *Sens. Actuat.* 4 (1983) 447–454.
- [25] H.C. Lim, B. Schulkin, M. Pulickal, S. Liu, R. Petrova, G. Thomas, S. Wagner, K. Sidhu, J.F. Federici, *Sens. Actuat. A-Phys.* 119 (2005) 332–335.
- [26] C. Iliescu, B. Chen, *J. Micromech. Microeng.* 18 (2007) 252–256.
- [27] R. Stree, *Technology and Applications of Amorphous Silicon*, Springer Science & Business Media, Berlin, 2013.
- [28] J. Joseph, S.G. Singh, S.R.K. Vanjari, *Mater. Lett.* 197 (2017) 52–55.
- [29] D.K. Tripathi, F. Jiang, M. Martyniuk, J. Antoszewski, K.D. Silva, J.M. Dell, L. Faraone, *J. Microelectromech. Syst.* 24 (2015) 1998–2007.
- [30] R.M. Pinto, P. Brito, V. Chu, J.P. Conde, *J. Microelectromech. Syst.* 28 (2019) 390–400.
- [31] H. Liao, K. Karki, Y. Zhang, J. Cumings, Y. Wang, *Adv. Mater.* 23 (2011) 4318–4322.
- [32] M. Závětová, J. Zemek, I. Akimchenko, *Czech. J. Phys. B* 31 (1981) 744–751.
- [33] B. Li, X. Tang, H. Xie, Z. Xin, In: *IEEE the Sixteenth International Conference on Micro Electro Mechanical Systems*, 2003.
- [34] S. Matsui, *Microsc. Microanal.* 12 (2000) 179–181.
- [35] U. Gösele, *Handbook of Ion Implantation Technology*, North-Holland, Amsterdam, 1992.
- [36] J.F. Ziegler, *Ion Implant. Sci. Technol.* 10 (1984) 51–108.
- [37] A. Lotnyk, D. Poppitz, U. Ross, J. Gerlach, F. Frost, S. Bernütz, E. Thelander, B. Rauschenbach, *Microelectron. Reliab.* 55 (2015) 2119–2125.
- [38] Y.B. Gerbig, C.A. Michaels, J.E. Bradby, B. Haberl, R.F. Cook, *Phys. Rev. B* 92 (2015) 214110.
- [39] T. Juliano, V. Domnich, Y. Gogotsi, *J. Mater. Res.* 19 (2004) 3099–3108.
- [40] D.E. Aspnes, A.A. Studna, *Phys. Rev. B* 27 (1983) 985.
- [41] A.S. Argon, M.J. Demkowicz, *Metall. Mater. Trans. A* 39 (2008) 1762–1778.
- [42] C.C. Wang, J. Ding, Y.Q. Cheng, J.C. Wan, L. Tian, J. Sun, Z.W. Shan, J. Li, E. Ma, *Acta Mater.* 60 (2012) 5370–5379.
- [43] F. Shimizu, S. Ogata, J. Li, *Acta Mater.* 54 (2006) 4293–4298.
- [44] W.F.V.D. Weg, A.J.M. Berntsen, F.W. Saris, A. Polman, *Mater. Chem. Phys.* 46 (1996) 140–146.
- [45] P. Zhang, I. Mitchell, B. Tong, P. Schultz, D. Lockwood, *Phys. Rev. B* 50 (1994) 17080.
- [46] J. Fabian, P.B. Allen, *Phys. Rev. Lett.* 79 (1997) 1885–1888.
- [47] C.A. Volkert, *J. Appl. Phys.* 70 (1991) 3521–3527.
- [48] A. Witvrouw, F. Spaepen, *J. Appl. Phys.* 74 (1993) 7154–7161.